ETH
Eidgenössische Technische Hochschule Zürich
Swiss Federal Institute of Technology Zurich

Efficient Calculation of the Wigner Potential in Crystal Systems Using the Ewald Method

Bachelor Thesis

G. Accaputo

Wednesday 11th March, 2015

Advisors: Prof. Dr. P. Hünenberger, Dr. M. Suter
Laboratory of Physical Chemistry, ETH Zürich

Abstract

The computation of electrostatic interactions in periodic systems of charges is a computationally expensive task due to the long-range nature of these interactions. The Ewald method speeds up such computations by splitting the long-range interaction into two contributions, evaluated in real and reciprocal space, respectively. The Wigner potential is a constant representing the self-energy of a charge and depends exclusively on the size and shape of the unit cell. The Ewald method provides a way to efficiently calculate the Wigner potential. In this thesis, the Wigner potential is analyzed based on different unit cells with the goal to find a simple analytical term accurately describing the Wigner potential. In a first part the Wigner potential is derived based on the Ewald method. Next, an implementation of the Wigner potential calculation using the Ewald method for general unit cells is discussed and provided. Since the convergence of the Wigner potential calculation depends on a specific parameter introduced by the Ewald method, the calculation of the optimal value for this specific parameter is examined, such that the convergence of the calculation and thus the correct numerical evaluation of the Wigner potential is guaranteed. Finally, the Wigner potential is analyzed based on the variation of the shape and size of the unit cell. For the fitting of the resulting curves models are provided based on nonlinear regression. Since the models provided for the curve fitting depend on multiple model parameters and the corresponding residues show trends, thus indicating the unsatisfactory quality of the models it is concluded that a simple analytical expression for the Wigner potential may not exist.

Acknowledgements

First and foremost, I offer my sincerest gratitude to my advisor Prof. Dr. Philippe Hünenberger for the possibility to work on this project, for providing me with the infrastructure in his lab, for his knowledge, patience and friendliness.

My sincere gratitude goes also to Dr. Martin Suter for his kindness, patience, his help throughout the whole project, his contributions to the poject and his assistance while writing the thesis.

Finally, I thank my parents for their loving support throughout all my studies and especially throughout this project.

Contents

Chapter 1

Introduction

The calculation and accurate treatment of electrostatic interactions in a molecular system is an essential requirement for performing a reliable explicit-solvent simulation of solvated molecules. Such biological systems of interest range in size from about a thousand to several thousands of molecules. Periodic boundary conditions are used to effectively represent the many properties of a bulk macroscopic system with a relatively small number of particles. The system is built from a simulation box surrounded by an infinite number of periodic copies of itself in all the three cartesian directions, completely filling the space. By applying periodic boundary conditions, surface effects arising from a finite size system and the resultant residing of a very substantial fraction of the particles on the surface are eliminated due to the infinite nature of the system.

The computation of electrostatic interactions requires the calculation of all the pair-wise interactions. The computational effort for this operation is proportional to the square of the number of particles, resulting in a computationally rather expensive task. This issue is particularly relevant in regard to the long-range part of intermolecular interactions (e.g. Coulombic interactions) in periodic systems. One way of solving the problem of the long-range interactions is the application of cutoff-based methods. Such methods introduce a shifting or scaling of Coulomb's law to force the Coulombic interactions to become negligible beyond a convenient distance defined by a cutoff radius. These approaches reduce the computational effort, but give rise to serious inaccuraces by altering the physical law. The effects on simulated quantities are difficult to anticipate, generating unsuitable approximations which are responsible for significantly modifying the energies and conformations sampled in a simulation [9].

Lattice-sum methods belong also to the family of methods used for the task of computing long-range interactions and have been successfully applied to calculate stable trajectories of solvated molecules in cases where cutoff-

based methods failed to do so [5]. A drawback of this method is that the electrostatic interactions are treated as exactly periodic. The periodicity also limits the accuracy of these methods due to errors committed during the numerical evaluation of the interactions [4]. Introducing periodicity may be reasonable for the simulation of crystals, but can lead to undesirable periodicity-induced artifacts in the simulations of solutions and may also have significant influence on the solvation of conformational properties of molecules [5]. Nonetheless, lattice-sum methods are commonly used for calculating long-range interactions. The Ewald method is a lattice-sum method that successfuly accelerates the calculation of the long-range interaction by dividing it into two parts: a short-range contribution which is calculated in real space and a long-range contribution which is calculated in Fourier space. The splitting itself introduces a constant called the Wigner potential, whose numerical value depends on the shape and size of the simulation box. In the particular case of a cubic unit cell of edge L, the numerical evaluation of the Wigner potential Ψ_{WI} leads to $\Psi_{WI} \approx -2.837297\, L^{-1}$ [5]. Since in practice unit cells other than the unit cube are used to construct various crystal systems, the goal of this thesis is to analyze the behaviour of the Wigner potential for different crystal systems and try to extract a simple analytical form of the potential, which then can be used to efficiently calculate the Wigner potential in simulations [6].

Chapter 2

Theory

This chapter introduces crystal systems, a concept used to describe various lattice systems. The issues arising from a periodic system of charges are discussed, followed by the presentation of a general periodic solution of the Poisson equation using Fourier series. Further, a solution for the electrostatic potential $\Phi(\mathbf{r})$ used for the physical problem consisting of periodic charges is shown. Most of the equations presented in this section are taken from [5]; equations taken from other sources are appropriately referenced in the text.

2.1 Periodic System of Charges

2.1.1 Crystal Lattice and Crystal Systems

For the representation of the periodic system of charges, the crystal lattice and crystal systems are introduced. For a crystal lattice, periodicity is defined by three generally non-orthogonal vectors $\mathbf{L}_1, \mathbf{L}_2, \mathbf{L}_3 \in \mathbb{R}^3$ [5]; the lattice itself is a collection of lattice points that can be generated by a set of discrete translation operations described by the vectors $\mathbf{L}_1, \mathbf{L}_2, \mathbf{L}_3$ and the components of the repeat vector $\mathbf{n} = (n_1, n_2, n_3)^\mathsf{T} \in \mathbb{Z}^3$:

$$\mathbf{r} = n_1\mathbf{L}_1 + n_2\mathbf{L}_2 + n_3\mathbf{L}_3 = \underline{\mathbf{L}}\,\mathbf{n} \quad . \tag{2.1}$$

The three-dimensional unit cell $\mathcal{C}$ is the smallest unit of volume in the crystal lattice that contains one or more atoms arranged in three-dimensions and is described by the matrix $\underline{\mathbf{L}}$, which is defined as $\underline{\mathbf{L}} = (\mathbf{L}_1, \mathbf{L}_2, \mathbf{L}_3) \in \mathbb{R}^{3\times3}$ and is referred to as the *unit cell size* [5]; the volume of $\mathcal{C}$ is denoted by

$$V = \det(\underline{\mathbf{L}}) \quad . \tag{2.2}$$

Table 2.1: Characteristics of the seven chrystal systems [1]

Structure	Edge Lengths	Angles between Edges
Cubic	$a = b = c$	$\alpha = \beta = \gamma = 90°$
Tetragonal	$a = b \neq c$	$\alpha = \beta = \gamma = 90°$
Orthorhombic	$a \neq b \neq c$	$\alpha = \beta = \gamma = 90°$
Hexagonal	$a = b \neq c$	$\alpha = \beta = 90°, \gamma = 120°$
Rhombohedral	$a = b = c$	$\alpha = \beta = \gamma \neq 90°$
Monoclinic	$a \neq b \neq c$	$\alpha = \gamma = 90°, \beta \neq 90°$
Triclinic	$a \neq b \neq c$	$\alpha \neq \beta \neq \gamma \neq 90°$

The positions of the atoms inside the unit cell can be represented in terms of fractional coordinates. The fractional coordinates corresponding to a Cartesian vector $\mathbf{q}$ are defined as the components of the vector $\mathbf{s} \in \mathbb{R}^3$ for which [5]

$$\mathbf{q} = \underline{\mathbf{L}}\,\mathbf{s} \quad . \tag{2.3}$$

The unit cell itself describes the bulk arrangement of the system. The complete crystal lattice can be constructed by a regular stacking of unit cells in a systematic fashion without overlapping and without gaps [7]. There are seven unique arrangements of unit cells, known as crystal systems, that can each be used to fill three-dimensional space [1]; these are cubic, tetragonal, orthorhombic, rhombohedral, hexagonal, monoclinic, and triclinic. In the case of the seven presented crystal systems, the unit cell $\mathcal{C}$ is a parallelepiped in shape with edge lengths a, b, c and angles α, β, γ between the edges [1] (Figure 2.1 and Table 2.1) and is characterized by the column vectors of the unit cell size $\underline{\mathbf{L}}$ [7]. For a parallelepiped $\mathcal{C}$, the specific unit cell size $\underline{\mathbf{L}}$ is given by [11]

$$\underline{\mathbf{L}} = \begin{bmatrix} a & b\cos(\gamma) & c\cos(\beta) \\ 0 & b\sin(\gamma) & c\frac{\cos(\alpha)-\cos(\beta)\cos(\gamma)}{\sin(\gamma)} \\ 0 & 0 & c\frac{v}{\sin(\gamma)} \end{bmatrix} \quad . \tag{2.4}$$

Further, the inverse matrix $\underline{\mathbf{L}}^{-1}$ can be written as [11]

$$\underline{\mathbf{L}}^{-1} = \begin{bmatrix} \frac{1}{a} & -\frac{\cos(\gamma)}{a\sin(\gamma)} & \frac{\cos(\alpha)\cos(\gamma)-\cos(\beta)}{av\sin(\gamma)} \\ 0 & \frac{1}{b\sin(\gamma)} & \frac{\cos(\beta)\cos(\gamma)-\cos(\alpha)}{bv\sin(\gamma)} \\ 0 & 0 & \frac{\sin(\gamma)}{cv} \end{bmatrix} \quad , \tag{2.5}$$

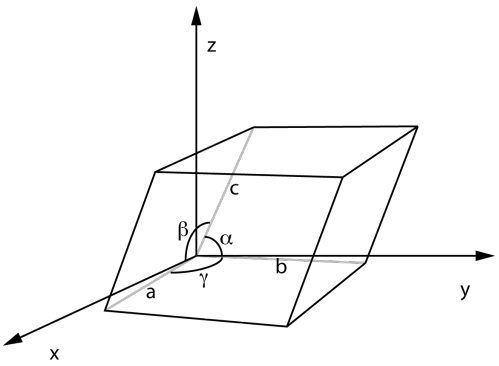

Figure 2.1: The unit cell $\mathcal{C}$ defined in terms of a parallelepiped with edge lengths a, b, c and the angles α, β, γ between the edges [2]

In both Eqs. 2.4 and 2.5, v is the volume of the unit parallelepiped and is defined as

$$v = \det(\tilde{\underline{\mathbf{L}}}) \quad , \tag{2.6}$$

where $\tilde{\underline{\mathbf{L}}}$ is the same as $\underline{\mathbf{L}}$ in Eq. 2.4, except for a, b, c are set explicitly to 1.

2.1.2 Issues Arising from a Periodic System of Charges

The infinite nature of the periodic system of charges represented by a crystal lattice gives raise to issues in regard to the calculation of the Coulomb interaction energy. To better understand these issues consider a system box represented by the unit cell $\mathcal{C}$ consisting of N_q point charges $\{q_i\}$ at locations $\{\mathbf{r}_i \in \mathcal{C}\}$ in vacuum, surrounded by an infinite number of periodic copies of itself. The total Coulomb interaction energy is [8]

$$E = \frac{1}{4\pi\varepsilon_0} \sum_{(i,j)} \frac{q_i q_j}{\|\mathbf{r}_i - \mathbf{r}_j\|} \quad , \tag{2.7}$$

where ε_0 is the vacuum permittivity and the sum is over all pairs (i, j). Since the system is subjected to periodic boundary conditions and the unit cell $\mathcal{C}$ is described by the three unit vectors $\mathbf{L}_1, \mathbf{L}_2, \mathbf{L}_3 \in \mathbb{R}^3$, if there is a point charge q_i at location $\mathbf{r}_i \in \mathcal{C}$, there are also point charges q_i called *periodic images of* q_i at

$$\mathbf{r}_i + n_1\mathbf{L}_1 + n_2\mathbf{L}_2 + n_3\mathbf{L}_3 = \mathbf{r}_i + \underline{\mathbf{L}}\,\mathbf{n} \quad , \tag{2.8}$$

with $\mathbf{n} = (n_1, n_2, n_3) \in \mathbb{Z}^3$. The total Coulomb interaction energy for a periodic system consisting of point charges has now to include the interactions

between an infinite number of charges [8]:

$$E = \frac{1}{4\pi\varepsilon_0} \sum_{\mathbf{n}\in\mathbb{Z}^3} \sum_{(i,j)} \frac{q_i q_j}{\|\mathbf{r}_i - \mathbf{r}_j + \underline{\mathbf{L}}\,\mathbf{n}\|} \quad . \tag{2.9}$$

The sum over all pairs can be rewritten into sums over all point charges [8]:

$$E = \frac{1}{4\pi\varepsilon_0} \frac{1}{2} \sum_{\mathbf{n}\in\mathbb{Z}^3} \sum_{i=1}^{N_q} \sum_{j=1}^{N_q}{}' \frac{q_i q_j}{\|\mathbf{r}_i - \mathbf{r}_j + \underline{\mathbf{L}}\,\mathbf{n}\|} \quad . \tag{2.10}$$

The $'$ symbol in Eq. 2.10 is used to denote that for the case $\mathbf{n} = \mathbf{0}$ the term $i = j$ is excluded from the sum; the factor $1/2$ instead is introduced to cancel out the double-counting. The infinite sum in Eq. 2.10 cannot be used to calculate the electrostatic energy in a simulation since the sum is conditionally convergent and the result therefore depends on the order of summation. In order to improve the convergence of the sum presented in Eq. 2.10, the expression for the charge density is rewritten in the following sections.

2.1.3 General Solution of the Poisson Equation Using Fourier Series

The electrostatic potential of a given system is governed by Poisson's equation. Before defining a solution for the electrostatic potential of the periodic system of charges, a general solution of the Poisson equation using Fourier series is derived in this section. In general, the Poisson equation can be written as

$$\nabla^2 f(\mathbf{r}) = -4\pi g(\mathbf{r}) \quad \Longleftrightarrow \quad \begin{cases} \nabla \cdot \mathbf{F}(\mathbf{r}) = -4\pi g(\mathbf{r}) \\ \nabla f(\mathbf{r}) = \mathbf{F}(\mathbf{r}) \end{cases} \quad . \tag{2.11}$$

The source density $g(\mathbf{r})$ and the vector function $\mathbf{F}(\mathbf{r})$ are required to be periodic functions, whereas for the function $f(\mathbf{r})$ this requirement does not necessarily have to hold [5]. The general solution of Eq. 2.11 can be written as

$$f(\mathbf{r}) = 4\pi V^{-1} \sum_{\mathbf{l}\in {}^t\mathbb{Z}^3,\, \|\mathbf{l}\|\neq 0} k^{-2}\, \hat{g}(\mathbf{k})\, \exp\{\mathrm{i}\mathbf{k}\mathbf{r}\} + \alpha \quad , \tag{2.12}$$

where $\hat{g}(\mathbf{k})$ are the Fourier coefficients of $g(\mathbf{r})$ and are calculated using Eq. A.2, and α is an extrinsic term. Further, the wavevector $\mathbf{k}$ is defined as

$\mathbf{k} = 2\pi \mathbf{l}\underline{\mathbf{L}}^{-1}$ and $k = \|\mathbf{k}\|$. ${}^t\mathbb{Z}^3$ denotes the space of row vectors with integer components; consequently, the product $\mathbf{l}\underline{\mathbf{L}}^{-1}$ is well-defined and $\mathbf{kr}$ can be interpreted as a matrix product. If the periodicity of $f(\mathbf{r})$ is a requirement, then both $\mathbf{F}_0$ and f_0 have to vanish, i.e. $\mathbf{F}_0 = \mathbf{0}$ and $f_0 = 0$ [5]. In this very case, the special solution for $f(\mathbf{r})$ is called the *influence function for a g-shaped source*.

Eq. 2.11 can be also solved with the use of a Green's function. By definition, a Green's function $G(\mathbf{r}, \mathbf{r}_0)$ is any solution of [10]

$$WG(\mathbf{r}, \mathbf{r}_0) = \delta(\mathbf{r} - \mathbf{r}_0) \quad , \tag{2.13}$$

where W is a linear differential operator, δ the Dirac delta function and $\mathbf{s}$ a point in the Euclidean space $\mathbb{R}^n$. For the solution of Eq. 2.11 consisting of a Green's function, a source density $\chi(\mathbf{r})$ is defined in terms of a periodic δ-shaped source density plus a homogeneous neutralizing background charge:

$$\chi(\mathbf{r}) = \delta_p(\mathbf{r}) - V^{-1} \quad . \tag{2.14}$$

$\delta_p(\mathbf{r})$ is the periodic Dirac delta function and is defined as

$$\delta_p(\mathbf{r}) = \sum_{\mathbf{n}\in\mathbb{Z}^3} \delta(\mathbf{r} + \underline{\mathbf{L}}\,\mathbf{n}) = \sum_{\mathbf{n}\in\mathbb{Z}^3} \frac{1}{4\pi r^2}\delta(\|\mathbf{r} + \underline{\mathbf{L}}\,\mathbf{n}\|) \quad , \tag{2.15}$$

with $\delta(\|\mathbf{r}\|) = \delta(r)$ being the one-dimensional and $\delta(\mathbf{r})$ the three-dimensional Dirac delta function respectively. The function $\Psi(\mathbf{r})$ is now a solution of

$$\nabla^2\Psi(\mathbf{r}) = -4\pi\,\chi(\mathbf{r}) = -4\pi\left[\delta_p(\mathbf{r}) - V^{-1}\right] \quad . \tag{2.16}$$

Since the periodicity of the solution $\Psi(\mathbf{r})$ of Eq. 2.16 is a requirement imposed by the physical problem at hand, $\Psi(\mathbf{r})$ should additionally satisfy the conditions [5]

$$\langle\Psi(\mathbf{r})\rangle_{\mathcal{C}} = V^{-1}\hat{\Psi}(\mathbf{0}) = 0 \quad , \tag{2.17a}$$

$$\langle\nabla\Psi(\mathbf{r})\rangle_{\mathcal{C}} = V^{-1}\widehat{\nabla\Psi}(\mathbf{0}) = \mathbf{0} \quad , \tag{2.17b}$$

where $\hat{\Psi}(\mathbf{k})$ are the Fourier coefficients of the solution $\Psi(\mathbf{r})$. By combining the general solution shown in Eq. 2.12 and the conditions from Eqs. 2.17a and 2.17b, the particular solution $\Psi(\mathbf{r})$ of Eq. 2.16 can be expressed as

$$\Psi(\mathbf{r}) = 4\pi V^{-1} \sum_{\mathbf{l}\in {}^t\mathbb{Z}^3,\, \|\mathbf{l}\|\neq 0} k^{-2} \exp\{\mathrm{i}\mathbf{k}\mathbf{r}\} \quad . \tag{2.18}$$

The solution $\Psi(\mathbf{r})$ (Eq. 2.18) resulting from Eq. 2.16 with the imposed conditions from Eqs. 2.17a and 2.17b is called the *influence function for a χ-shaped source*. The Fourier coefficients of the function $f(\mathbf{r})$ in Eq. 2.12 with $\alpha = 0$ are defined as

$$\hat{f}(\mathbf{k}) = 4\pi k^{-2} \hat{g}(\mathbf{k})[1 - \delta_{\mathbf{k}}] \quad , \tag{2.19}$$

where $\delta_{\mathbf{k}}$ is the Kronecker delta, i.e. $\delta_{\mathbf{k}} = 0 \Leftrightarrow \mathbf{k} = \mathbf{0}$ and $\delta_{\mathbf{k}} = 1$ otherwise. In addition, the Fourier coefficients of $\Psi(\mathbf{r})$ from Eq. 2.18 are given by

$$\hat{\Psi}(\mathbf{k}) = 4\pi k^{-2}[1 - \delta_{\mathbf{k}}] \quad . \tag{2.20}$$

By combining Eqs. 2.19 and 2.20, $\hat{f}(\mathbf{k})$ from Eq. 2.19 can be rewritten as

$$\hat{f}(\mathbf{k}) = \hat{g}(\mathbf{k})\hat{\Psi}(\mathbf{k}) \quad . \tag{2.21}$$

Since $\hat{f}(\mathbf{k})$ in Eq. 2.21 is a multiplication of the Fourier coefficients of $\Psi(\mathbf{r})$ and $g(\mathbf{r})$, taking into consideration Eqs. A.3 and A.4 the general solution for $f(\mathbf{r})$ is simply the convolution $(g \star \Psi)(\mathbf{r})$ and is thus given by

$$f(\mathbf{r}) = \int\int\int_{\mathcal{C}} \mathrm{d}^3\mathbf{r}'\, g(\mathbf{r}')\, \Psi(\mathbf{r} - \mathbf{r}') \quad , \tag{2.22}$$

with $\Psi(\mathbf{r})$ being the Green's function for the Poisson equation under periodic boundary conditions [5].

2.1.4 The Electrostatic Potential

Considering the approach presented in the previous section for finding a general periodic solution of Poisson's equation, the goal of this section is to define a specific solution of Poisson's equation for the electrostatic potential $\Phi(\mathbf{r})$ in a periodic system of charges. Generally, in a periodic or non-perodic system, the electrostatic potential $\Phi(\mathbf{r})$ is a solution of

$$\nabla^2\Phi(\mathbf{r}) = -\frac{1}{\varepsilon_0}\rho(\mathbf{r}) \quad , \tag{2.23}$$

where $\rho(\mathbf{r})$ is the charge density in the system. The charge density $\rho_i(\mathbf{r})$ for a point charge q_i is

$$\rho_i(\mathbf{r}) = q_i\delta(\mathbf{r} - \mathbf{r}_i) \quad . \tag{2.24}$$

Under non-periodic boundary conditions, the charge density reads

$$\rho_{NP}(\mathbf{r}) = \sum_{i=1}^{N_q} q_i\delta(\mathbf{r} - \mathbf{r}_i) \quad . \tag{2.25}$$

The expression $\rho_{NP}(\mathbf{r})$ can be generalized under periodic boundary conditions by replacing $\delta(\mathbf{r})$ with the periodic point charge plus homogeneous neutralizing background charge $\chi(\mathbf{r})$defined in Eq. 2.14 [5]; the charge density under periodic boundary conditions may be now written as

$$\rho(\mathbf{r}) = \sum_{i=1}^{N_q} q_i\,\chi(\mathbf{r} - \mathbf{r}_i) \quad . \tag{2.26}$$

By defining the quantity

$$S_{\mathcal{C}} = \sum_{i=1}^{N_q} q_i \tag{2.27}$$

representing the charge of the unit cell and the function $s(\mathbf{r})$ as

$$s(\mathbf{r}) = \sum_{i=1}^{N_q} q_i\,\delta_p(\mathbf{r} - \mathbf{r}_i) \quad , \tag{2.28}$$

the charge density can be rewritten to

$$\rho(\mathbf{r}) = s(\mathbf{r}) - V^{-1}S_{\mathcal{C}} \quad . \tag{2.29}$$

By combining Eq. 2.23 and Eq. 2.29, the periodic electrostatic potential $\Phi(\mathbf{r})$ must be a solution of

$$\nabla^2\Phi(\mathbf{r}) = \rho(\mathbf{r}) = s(\mathbf{r}) - V^{-1}S_{\mathcal{C}} \quad . \tag{2.30}$$

Since Eq. 2.30 consists of a δ-shaped source term, as mentioned in section 2.1.3 it is suitable to use a Green's function for the solution of this equation. The general solution of Eq 2.30 is therefore given by

$$\Phi(\mathbf{r}) = \frac{1}{4\pi\varepsilon_0}\int\int\int_{\mathcal{C}} \mathrm{d}^3\,\mathbf{r}'\Psi(\mathbf{r}-\mathbf{r}')s(\mathbf{r}') + \Phi_{ext}(\mathbf{r}) \quad , \tag{2.31}$$

where $\Psi(\mathbf{r})$ is a Green's function under periodic boundary condition and $\Phi_{ext}(\mathbf{r})$ being the extrinsic potential. The detailed derivation of the solution of Eq. 2.31 and a definition of $\Phi_{ext}(\mathbf{r})$ are shown elsewhere [5].

The electrostatic free energy ΔG_{el} represents the work required to reversibly charge the system and is defined as

$$\Delta G_{el} = \Delta G_{int} + \Delta G_{ext} \quad , \tag{2.32}$$

with

$$\Delta G_{int} = \frac{1}{8\pi\varepsilon_0}\int\int\int_{\mathcal{C}} \mathrm{d}^3\mathbf{r}s(\mathbf{r})\int\int\int_{\mathcal{C}} \mathrm{d}^3\mathbf{r}'\tilde{\Psi}(\mathbf{r}-\mathbf{r}')s(\mathbf{r}') \quad . \tag{2.33}$$

Since ΔG_{int} originally is an infinite quantity due to the infinite Coulombic self-energy at a point charge, the Green's function $\Psi(\mathbf{r})$ is replaced by the following non-singular Green's function $\tilde{\Psi}(\mathbf{r})$ in Eq. 2.33 to make ΔG_{int} a finite quantity [5]:

$$\tilde{\Psi}(\mathbf{r}) = \begin{cases} \Psi(\mathbf{r}) & \mathbf{r} \neq \mathbf{0} \\ \Psi_{WI} = \lim_{\mathbf{r}\to\mathbf{0}}\left[\Psi(\mathbf{r}) - \frac{1}{r}\right] & \mathbf{r} = 0 \end{cases} \quad . \tag{2.34}$$

The term Ψ_{WI} is a constant related to the Wigner potential and depends exclusively on the shape and size of the unit cell [5].

2.2 The Ewald Method

Since the direct summation of Eq. 2.10 is impracticable due to the slowly decaying long-range part of the Coulomb potential and the singularity at the origin, the goal of this section is to explain how the convergence of the sum presented in Eq. 2.10 can be improved with the help of the Ewald method [5]. The idea behind the Ewald method is to separate both the difficulties mentioned in the beginning of this section into two parts by using the following identity:

$$\frac{1}{r} = \eta(r) + \left[\frac{1}{r} - \eta(r)\right] \quad . \tag{2.35}$$

$\eta(r)$ contains the singularity and is required to be short-ranged (vanishing exponentially as $r \to \infty$), whereas $\left[\frac{1}{r} - \eta(r)\right]$ is long-ranged and required to be non-singular and slowly varying for all r. For the long-ranged part of Eq. 2.35, the choice of a slowly varying function has the advantage that its Fourier transform can be represented accurately by only a few $\mathbf{k}$ vectors and therefore permits an efficient calculation of the long-ranged contribution in Fourier space [5].

2.2.1 Splitting the Charge Distribution $\chi(\mathbf{r})$

In this section the approach presented in Eq. 2.35 is applied on the charge distribution $\chi(\mathbf{r})$ from Eq. 2.14. $\chi(\mathbf{r})$ as presented in Eq. 2.14 can be split by adding and subtracting a smooth and slowly varying distribution $\gamma_p(\mathbf{r})$:

$$\chi(\mathbf{r}) = \delta_p(\mathbf{r}) - V^{-1} = \chi_S(\mathbf{r}) + \chi_L(\mathbf{r}) \quad , \tag{2.36a}$$
$$\chi_S(\mathbf{r}) = \delta_p(\mathbf{r}) - \gamma_p(\mathbf{r}) \quad , \tag{2.36b}$$
$$\chi_L(\mathbf{r}) = \gamma_p(\mathbf{r}) - V^{-1} \quad , \tag{2.36c}$$

with $\chi_S(\mathbf{r})$ denoting the short-ranged and $\chi_L(\mathbf{r})$ the long-ranged contribution to the charge density $\chi(\mathbf{r})$ respectively. $\gamma_p(\mathbf{r})$ is defined as

$$\gamma_p(\mathbf{r}) = \sum_{\mathbf{n}\in\mathbb{Z}^3} \gamma_n(\|\mathbf{r} + \underline{\mathbf{L}}\,\mathbf{n}\|) \quad , \tag{2.37}$$

with the one-dimensional function $\gamma_n(r)$ being the *charge-shaping function*. Although the charge-shaping function γ_n is historically taken to be a normalized spherical Gaussian, this choice comes with some drawbacks; the

evaluation of the exponential and error functions arising from the use of a Gaussian is a computationally expensive task and since the Gaussian function is not finite-ranged, the selection of a specific Gaussian width has a strong influence on the accuracy [4]. It has been shown in [4] that employing polynomials truncated to a finite spacial range as charge-shaping functions leads, amongst other things, to improvements in terms of accuracy and computational efficiency. One of these truncated polynomials is the *normalized spherical hat function* and is defined as

$$\gamma_n(r) = (\pi/3\,d^4)^{-1}(d-r)H(d-r) \quad , \tag{2.38}$$

where d is the width of the truncated polynomial and $H(x)$ the discrete Heaviside step function, i.e. $H(x) = 1 \Leftrightarrow x \geq 0$ and $H(x) = 0$ otherwise.

2.2.2 Splitting the Influence Function $\Psi(\mathbf{r})$

The influence function $\Psi(\mathbf{r})$ given as a solution of Eq. 2.16 is recovered in this section by considering the splitted charge distribution $\chi(\mathbf{r})$ as defined in Eq. 2.36a. The normalized spherical hat function γ_n presented in Eq. 2.38 is used as the charge-shaping function for further calculations; γ_p from Eq. 2.37 is now explicitly defined as

$$\gamma_p(\mathbf{r}) = \sum_{\mathbf{n}\in\mathbb{Z}^3} (\pi/3\,d^4)^{-1}(d - \|\mathbf{r} + \underline{\mathbf{L}}\,\mathbf{n}\|)H(d - \|\mathbf{r} + \underline{\mathbf{L}}\,\mathbf{n}\|) \quad . \tag{2.39}$$

An analog equation to Eq. 2.16 is constructed by replacing the singular function $\delta_p(\mathbf{r})$ with the smoother distribution $\gamma_p(\mathbf{r})$:

$$\nabla^2\Psi_L(\mathbf{r}) = -4\pi\,\chi_L(\mathbf{r}) = -4\pi\left[\gamma_p(\mathbf{r}) - V^{-1}\right] \quad . \tag{2.40}$$

By imposing the conditions [5]

$$\langle\Psi_L(\mathbf{r})\rangle_{\mathcal{C}} = 0 \qquad \text{and} \qquad \langle\nabla\Psi_L(\mathbf{r})\rangle_{\mathcal{C}} = \mathbf{0} \tag{2.41}$$

on Eq. 2.40, the solution resulting from Eq. 2.40 is the influence function $\Psi_L(\mathbf{r})$ for the periodic γ-shaped source plus homogeneous neutralizing background and can be expressed as

$$\Psi_L(\mathbf{r}) = 4\pi V^{-1} \sum_{\mathbf{l}\in\,{}^t\mathbb{Z}^3,\,\|\mathbf{l}\|\neq 0} k^{-2}\,\hat{\gamma}_p(k)\exp\{\mathrm{i}\mathbf{k}\mathbf{r}\} \quad , \tag{2.42}$$

with

$$\hat{\gamma}_p(k) = 12(dk)^4(2 - 2\cos(dk)) - dk\sin(dk)) \tag{2.43}$$

being the Fourier coefficients of $\gamma_p(\mathbf{r})$ defined in Eq. 2.39 [5]. $\Psi_L(\mathbf{r})$ is the long-ranged (non-singular) contribution to the electrostatic potential and is evaluated in Fourier space. The aim now is to recover the Green's function $\Psi(\mathbf{r})$ for the periodic δ-shaped source plus homogeneous neutralizing background defined in Eq. 2.30 by correcting $\Psi_L(\mathbf{r})$ using the following equation:

$$\Psi(\mathbf{r}) = \Psi_L(\mathbf{r}) + \Psi_S(\mathbf{r}) + A_1 \quad . \tag{2.44}$$

$\Psi_S(\mathbf{r})$ accounts for the short-ranged (singular) correction to $\Psi_L(\mathbf{r})$ and is defined as the solution of

$$\nabla^2\Psi_S(\mathbf{r}) = -4\pi\,\chi_S(\mathbf{r}) = -4\pi\left[\delta_p(\mathbf{r}) - \gamma_p(\mathbf{r})\right] \quad . \tag{2.45}$$

The general solution $\Psi_S(\mathbf{r})$ of Eq. 2.45 is given by

$$\Psi_S(\mathbf{r}) = \eta(\|\mathbf{r} + \underline{\mathbf{L}}\,\mathbf{n}\|) + \sum_{\mathbf{n}\in\mathbb{Z}^3,\,\|\mathbf{n}\|\neq 0} \eta(\|\underline{\mathbf{L}}\,\mathbf{n}\|) \quad . \tag{2.46}$$

In the case of the normalized spherical hat function in Eq. 2.38, $\eta(r)$ is defined as

$$\eta(r) = (r^{-1} + 1/2a^{-3}r^2 - 3/2a^{-1})H(d - r) \quad . \tag{2.47}$$

The term A_1 in Eq. 2.44 is needed to satisfy the requirements $\langle\Psi(\mathbf{r})\rangle_{\mathcal{C}} = \langle\Psi_L(\mathbf{r})\rangle_{\mathcal{C}} = 0$ [5] and is therefore expressed as

$$A_1 = -\langle\Psi_S(\mathbf{r})\rangle_{\mathcal{C}} = -4\pi V^{-1}\int_0^\infty \mathrm{d}r\, r^2\,\eta(r) \quad . \tag{2.48}$$

Using the definition of $\eta(r)$ shown in Eq. 2.47, the term A_1 from Eq. 2.48 evaluates to [5]

$$A_1 = -4/15\pi d^2 V^{-1} \tag{2.49}$$

in the case of the normalized spherical hat function in Eq. 2.38.

2.2.3 The Wigner Potential

A general expression for the Wigner term Ψ_{WI} shown in Eq. 2.34 is derived in this section using the normalized spherical hat function γ_n presented in Eq. 2.38. In Eq. 2.34 the constant Ψ_{WI} is defined as

$$\Psi_{WI} = \lim_{\mathbf{r}\to\mathbf{0}} \left[\Psi(\mathbf{r}) - \frac{1}{r} \right] \quad . \tag{2.50}$$

By replacing $\Psi(\mathbf{r})$ in Eq. 2.50 with $\Psi(\mathbf{r})$ from Eq. 2.44 and additionally defining [5]

$$A_2 = \Psi_L(\mathbf{0}) \quad , \tag{2.51}$$

$$A_3 = \lim_{\mathbf{r}\to\mathbf{0}} \left[\Psi_S(\mathbf{r}) - r^{-1} \right] \quad , \tag{2.52}$$

Eq. 2.50 can be rewritten to

$$\Psi_{WI} = A_1 + A_2 + A_3 \quad . \tag{2.53}$$

Using Eq. 2.40, A_2 in Eq. 2.51 can be expressed as

$$A_2 = 4\pi V^{-1} \sum_{\mathbf{l}\in {}^t\mathbb{Z}^3,\, \|\mathbf{l}\|\neq 0} k^{-2}\, \hat{\gamma}_p(k) \quad , \tag{2.54}$$

with $\hat{\gamma}_p(k)$ being defined in Eq. 2.43. Further, A_3 in Eq. can be written as

$$A_3 = -4\pi \int_0^\infty \mathrm{d}r\, \gamma_n(r) \quad . \tag{2.55}$$

Evaluating A_3 for the normalized spherical hat function in Eq. 2.38 results in [5]

$$A_3 = -2d^{-1} \quad . \tag{2.56}$$

Finally, by combining Eqs. 2.49, 2.50, 2.54 and 2.56, Ψ_{WI} can be numerically evaluated by using

$$\Psi_{WI} = -4/15\pi d^2 V^{-1} + 4\pi V^{-1} \left[\sum_{\mathbf{l} \in {}^t\mathbb{Z}^3,\, \|\mathbf{l}\| \neq 0} k^{-2}\, \hat{\gamma}_p(k) \right] - 2d^{-1} \quad . \qquad (2.57)$$

The Wigner term Ψ_{WI} depends exclusively on the shape and size of the unit cell, and in the particular case of a cubic unit cell of edge L, numerical evaluation leads to $\Psi_{WI} = \xi_{EW} L^{-1} \approx -2.837297\, L^{-1}$ [5].

Chapter 3

Methods

3.1 Implementation of the Wigner Potential Calculation in Crystal Systems Using the Ewald Method

The implementation of the Wigner potential calculation based on the Ewald method derived in Chapter 2.2.3 and shown in Eq. 2.57 is discussed in this section. Since the expression for Ψ_{WI} in Eq. 2.57 contains a sum consisting of infinitely many terms, the parameter $l_{\max} \in \mathbb{N}$ with $l_{\max} < \infty$ was introduced to limit the number of terms for the evaluation of the aforementioned sum in the implementation [3]. Let $\mathcal{L}$ be the set of row vectors $\mathbf{l}$ defined as [3]

$$\mathcal{L} := \{\mathbf{l} = (l_1, l_2, l_3) : l_i \in [-l_{\max}, l_{\max}] \text{ for } i = 1,2,3 \text{ and } \mathbf{l} \neq \mathbf{0},\ \|\mathbf{l}\|^2 \leq l_{\max}^2\} \quad . \tag{3.1}$$

Using the definition of $\mathcal{L}$ presented in Eq. 3.1, the expression for the Wigner potential Ψ_{WI} from Eq. 2.57 can be now rewritten as follows to be used in the implementation:

$$\Psi_{WI} \approx -4/15\pi d^2 V^{-1} + 4\pi V^{-1} \left[\sum_{\mathbf{l} \in \mathcal{L}} k^{-2}\, \hat{\gamma}_p(k) \right] - 2d^{-1} \quad . \tag{3.2}$$

The implementation of the Wigner potential calculation in crystal systems using the Ewald method is provided in Listing A.2; Eq. 3.2 was implemented in Listing A.2 to calculate the Wigner potential Ψ_{WI}, with $\hat{\gamma}_p$ being defined in Eq. 2.43 and d being the width of the normalized spherical hat function γ_n shown in Eq. 2.38. Furthermore, the implementation shown in Listing A.2 accepts a general unit cell size $\underline{\mathbf{L}} \in \mathbb{R}^{3\times3}$ as a parameter and since in Chapter 2.1.3 k was defined as $k = \|\mathbf{k}\| = \|2\pi\mathbf{l}\underline{\mathbf{L}}^{-1}\|$, for the calculation of the matrix

inverse $\underline{\mathbf{L}}^{-1}$ of $\underline{\mathbf{L}}$ Cramer's rule for 3×3 matrices was implemented [14]. An implementation of the Wigner potential calculation in a crystal system represented by a cubic unit cell of length L using the direct sum [3]

$$\Psi_{WI} \approx 4\pi V^{-1} \left(\left[\sum_{\mathbf{l} \in \mathcal{L}} k^{-2} \right] - L^2 \, l_{\max} / \pi \right) \tag{3.3}$$

is shown in Listing A.1 and was provided at the beginning of the project [6], where L is the length and $V = L^3$ the volume of the cubic unit cell, and the set $\mathcal{L}$ is defined in Eq. 3.1. Both methods for the calculation of the Wigner potential from Listings A.1 and A.2 were compared in terms of convergence.

3.2 Calculation of the Optimal Width d of the Normalized Spherical Hat Function γ_n

In this section an approach for the calculation of the optimal value of the width d for the normalized spherical hat function γ_n (Eq. 2.38) is presented. The actual choice of d in Eqs. 2.38 and 2.57 has influence on the convergence and therefore the numerical evaluation of the Wigner potential Ψ_{WI}; with the right choice of d in Eq. 2.38, the correct numerical evaluation of Ψ_{WI} for a given unit cell is achieved [6]. The optimal value d_{opt} that the parameter d in Eq. 2.38 should take is defined as the distance to the nearest periodic neighbour of a charge [6]; in the case of a cubic unit cell of length L, the optimal value is defined as $d_{\text{opt}} = L$. Let $\mathcal{P}$ be the unit cell represented by a parallelepiped as described in Chapter 2.1.1 (see Figure 2.1). Although a charge placed at $\mathbf{q} \in \mathcal{P}$ has infinitely many periodic images of itself spread throughout the crystal system, in three dimensions it has exactly 26 directly neighbouring periodic images which come into consideration for the calculation of the optimal value d_{opt}; these neighbours are referred to as the *direct neighbours of* $\mathbf{q}$ in this thesis. The charge $\mathbf{q}$ itself is placed at the origin of the coordinate system, i.e. $\mathbf{q} = \mathbf{0}$. $\mathcal{N} := \{\mathbf{n} = (n_1, n_2, n_3)^\intercal : n_i \in \{-1, 0, 1\} \text{ for } i = 1, 2, 3 \text{ and } \mathbf{n} \neq \mathbf{0}\}$ represents the set of repeat vectors needed to define the positions of the direct neighbours of $\mathbf{q}$ with $|\mathcal{N}| = 26$; Eq. A.1.3 lists the complete set $\mathcal{N}$. Further, let $\mathcal{V}_\mathbf{q} := \{\mathbf{v} = (v_1, v_2, v_3)^\intercal \in \mathbb{R}^3\}$ be the set of coordinate vectors of all direct neighbours of $\mathbf{q}$; using Eq. 2.8, $\mathbf{v}_j \in \mathcal{V}_\mathbf{q}$ is then defined as

$$\mathbf{v}_j = \mathbf{q} + \underline{\mathbf{L}} \, \mathbf{n}_j \quad \text{for} \quad j = 1, \ldots, 26 \quad , \tag{3.4}$$

with $\mathbf{n}_j \in \mathcal{N}$. Since the optimal value d_{opt} is defined as the shortest Euclidean distance between $\mathbf{q}$ and its direct neighbours $\mathbf{v}_j \in \mathcal{V}_\mathbf{q}$, d_{opt} can now be expressed as

$$d_{\text{opt}} = \min_{\mathbf{v}_j \in \mathcal{V}_\mathbf{q}} \|\mathbf{v}_j - \mathbf{q}\| \quad . \tag{3.5}$$

The calculation of d_{opt} based on a parallelepiped unit cell $\mathcal{P}$ with edge lengths a, b, c and the angles α, β, γ between the edges is presented in Listing A.3. A system depicting the neighbourhood of a single charge $\mathbf{q} \in \mathcal{P}$ placed at the origin surrounded by its 26 direct neighbours as described in Eq. 3.4 is constructed in the implementation; d_{opt} as defined in Eq. 3.5 is then determined by calculating the Euclidean distance to each direct neighbour and taking the smallest resulting value.

3.3 Analysis of the Wigner Potential Ψ_{WI} Based on the Variation of Shape and Size of the Unit Cell

The objective was to analyze the behaviour of the Wigner potential Ψ_{WI} based on the variation of the underlying parallelepiped unit cell, since Ψ_{WI} depends exclusively on the shape and size of the unit cell [5]. From this analysis the goal was to find a simple analytical expression for the Wigner potential Ψ_{WI} as a function of the unit cell size $\underline{\mathbf{L}}$. The behaviour of Ψ_{WI} was analyzed in a first part by only varying the edge length c of the parallelepiped unit cell and evaluating Ψ_{WI} for different values of c (with $a = b = 1, \alpha = \beta = \gamma = 90°$); in a second part Ψ_{WI} was evaluated at various different values for the angle γ of the unit cell (with $a = b = c = 1, \alpha = \beta = 90°$).

Chapter 4

Results

4.1 Convergence of the Wigner Potential Calculation in Crystal Systems Using the Ewald Method

In this section the convergence of both implementations of the Wigner potential calculation presented in Chapter 3.1 is discussed. The numerical evaluation of the Wigner potential Ψ_{WI} for a crystal system represented by a cubic unit cell of length L results in $\Psi_{WI} \approx -2.837297\, L^{-1}$ [5]. To compare both methods from Listings A.1 and A.2 in regard to the calculation of the Wigner potential, a cubic unit cell with $L = 1$ ($a = b = c = 1$; see Table 2.1) was used and $l_{\max}$ was arbitrarly set to $l_{\max} = 545$; in the case of the cubic unit cell with $L = 1$, the Wigner potential should evaluate to the expected value

$$\Psi_{WI} \approx -2.837297 \quad . \tag{4.1}$$

In the following lines, the Wigner potential calculated by the method from Listing A.1 is denoted as $\Psi_{WI,DS}$ and the Wigner potential calculated by the method from Listing A.2 as $\Psi_{WI,EW}$. Figure 4.1 shows that the absolute error $\Delta\Psi_{WI}$ between $\Psi_{WI,EW}$ and Ψ_{WI} (Eq 4.1) defined as $\Delta\Psi_{WI} = |\Psi_{WI} - \Psi_{WI,EW}|$ (red line) vanishes rather fast; the absolute error $\Delta\Psi_{WI} = |\Psi_{WI} - \Psi_{WI,DS}|$ (blue line) however does not vanish at all for $l_{\max} = 545$; Figure 4.1 confirms the rather fast convergence of the Wigner potential calculation using the Ewald method implementation shown in Listing A.2 compared to the calculation using the direct sum implementation in Listing A.1.

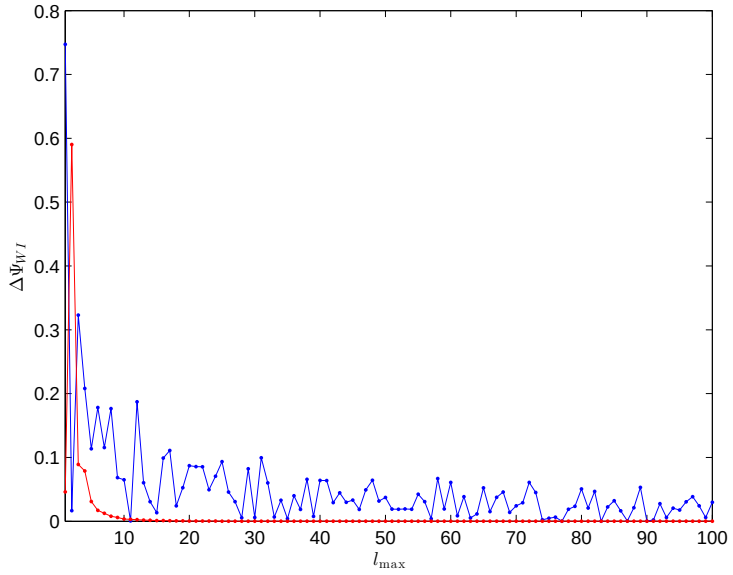

Figure 4.1: Absolute error $\Delta\Psi_{WI}$ between the Wigner potential calculated by both methods from Listings A.1 (blue line; direct sum method) and A.2 (red line; Ewald method) with a cubic unit cell of length $L = 1$ ($l_{\max} = 545$) and the expected Wigner potential $\Psi_{WI} \approx -2.837297$. The red line has been magnified by a factor 100 to emphasize the rather fast convergence of the Ewald method implemented in Listing A.2

4.2 Convergence of the Wigner Potential Calculation Based on the Choice of Width d of the Normalized Spherical Hat Function γ_n

The calculation of d_{opt} as derived in Chapter 3.2 and implemented in Listing A.3 was tested with different cubic, tetragonal, orthorhombic, rhombohedral, monoclinic, and triclinic unit cells (Table 2.1). Figures 4.2, 4.3, 4.5, 4.4, 4.6, and 4.7 show the absolute error $\Delta\Psi_{WI}$ between the correct Wigner potential Ψ_{WI} calculated with the optimal width d_{opt} [6] and Ψ_{WI} calculated with a varying width d for the respective shape of the unit cell using $l_{\max} = 300$; each of the plots shows as expected an increase of the absolute error $\Delta\Psi_{WI}$ for $d > d_{\text{opt}}$, describing a divergence and thus a wrong numerical evaluation of Ψ_{WI} for $d > d_{\text{opt}}$. The results confirm that using $d = d_{\text{opt}}$ for the calculation of Ψ_{WI} defined in Eq. 3.2 is advised, resulting in the correct numerical evaluation of Ψ_{WI} as expected [6].

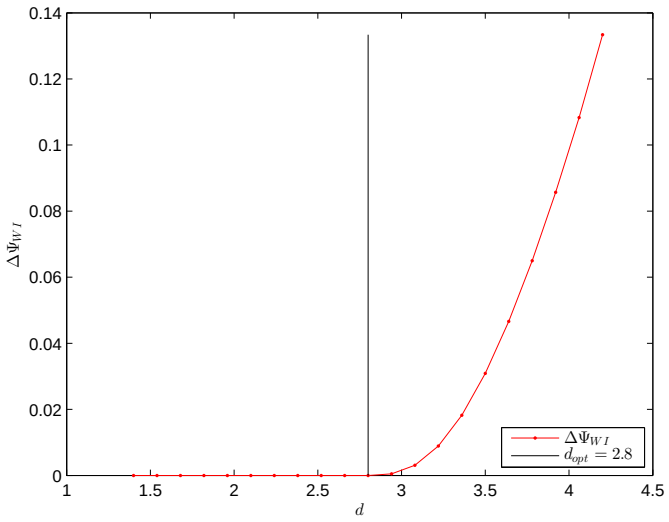

Figure 4.2: Absolute error $\Delta\Psi_{WI}$ between the Wigner potential Ψ_{WI} calculated with the optimal width d_{opt} [6] and Ψ_{WI} calculated with a varying width d for a cubic unit cell with edge lengths $a = b = c = 2.8$ (Table 2.1)

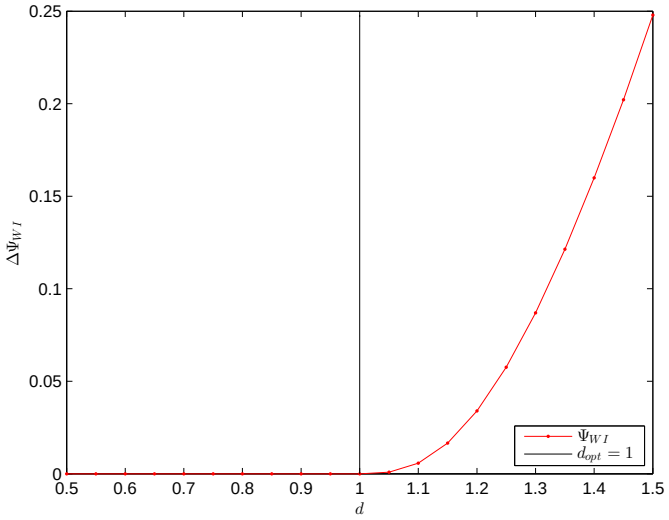

Figure 4.3: Absolute error $\Delta\Psi_{WI}$ between the Wigner potential Ψ_{WI} calculated with the optimal width d_{opt} [6] and Ψ_{WI} calculated with a varying width d for a tetragonal unit cell with edge lengths $a = b = 1, c = 3.8$ (Table 2.1)

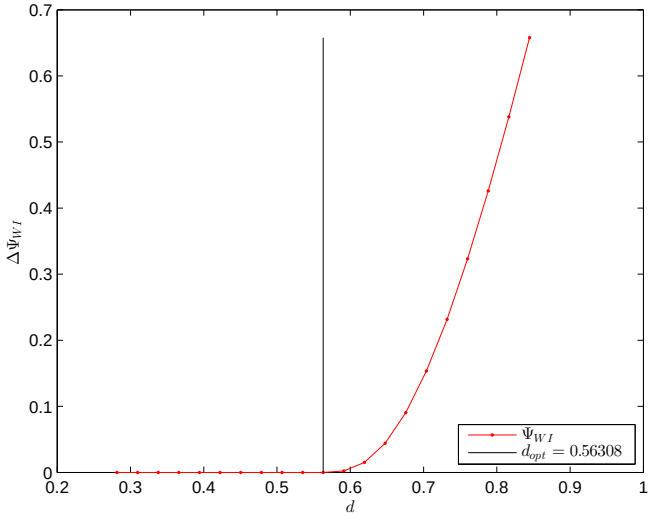

Figure 4.4: Absolute error $\Delta\Psi_{WI}$ between the Wigner potential Ψ_{WI} calculated with the optimal width d_{opt} [6] and Ψ_{WI} calculated with a varying width d for a rhombohedral unit cell with edge lengths $a = 1, b = 1, c = 1$ and angles $\alpha = \beta = \gamma \approx 32.7042°$ (Table 2.1)

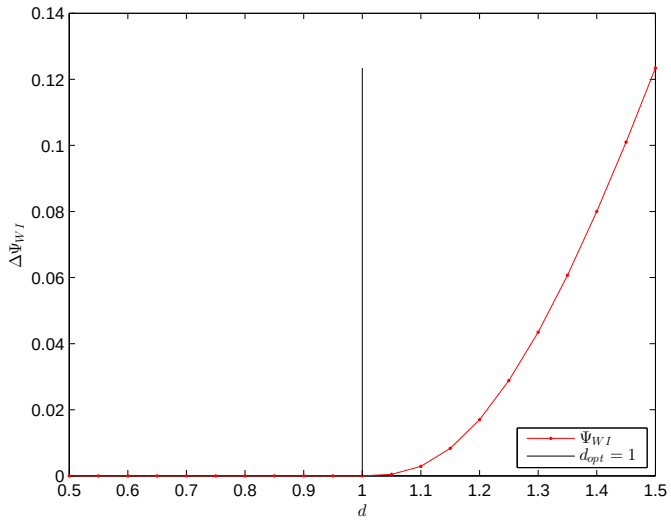

Figure 4.5: Absolute error $\Delta\Psi_{WI}$ between the Wigner potential Ψ_{WI} calculated with the optimal width d_{opt} [6] and Ψ_{WI} calculated with a varying width d for a orthorhombic unit cell with edge lengths $a = 1, b = 2.8, c = 3$ (Table 2.1)

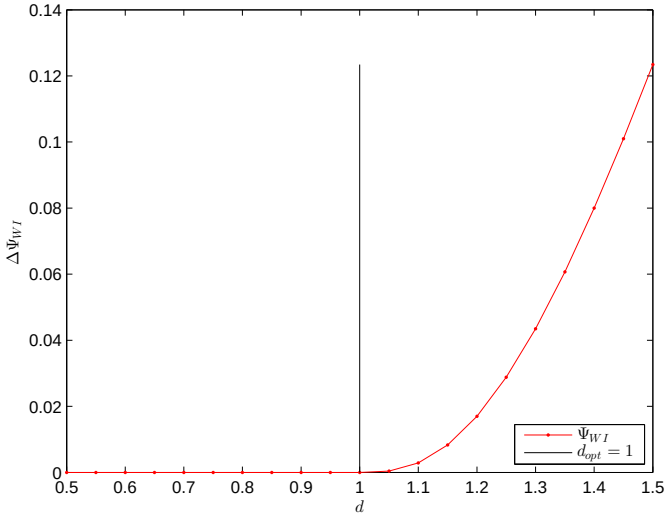

Figure 4.6: Absolute error $\Delta\Psi_{WI}$ between the Wigner potential Ψ_{WI} calculated with the optimal width d_{opt} [6] and Ψ_{WI} calculated with a varying width d for a monoclinic unit cell with edge lengths $a = 1, b = 3.8, c = 4$ and angle $\beta \approx 32.7042°$ (Table 2.1)

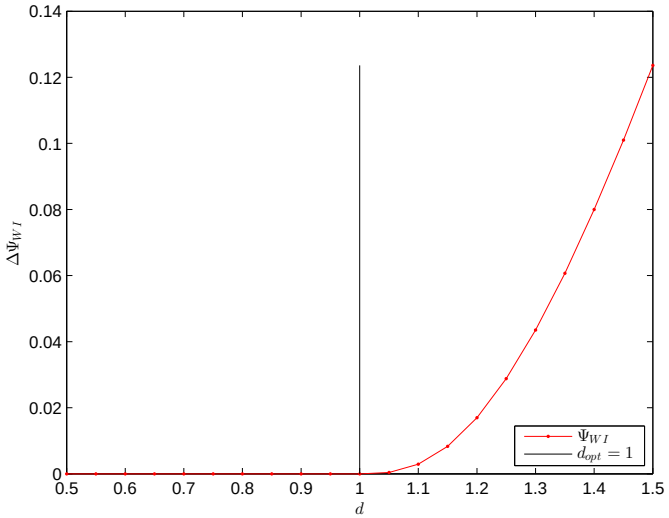

Figure 4.7: Absolute error $\Delta\Psi_{WI}$ between the Wigner potential Ψ_{WI} calculated with the optimal width d_{opt} [6] and Ψ_{WI} calculated with a varying width d for a triclinic unit cell with edge lengths $a = 1, b = 3.8, c = 4$ and angles $\alpha \approx 32.7042°, \beta \approx 26.9746°, \gamma \approx 21.2450°$ (Table 2.1)

4.3 Behaviour of the Wigner Potential Ψ_{WI} Based on the Variation of Shape and Size of the Unit Cell

In Figure 4.14 the behaviour of Ψ_{WI} (Eq. 3.2) with varying edge length $c \in [0, 10]$ of the parallelepiped unit cell with the edge lengths $a = b = 1$ and the angles $\alpha = \beta = \gamma = 90°$ is shown. The graph displayed in Figure 4.14 shows a rather interesting behaviour for smaller values of c in the interval $[0, 2]$ and seems to remain steady for large enough values of c. In the latter case, a linear regression suggests that Ψ_{WI} behaves like $\Psi_{WI}(c) = 1.0472\,c - 3.9003$ for $c \in (2, 10]$, with a rather small residual sum of squares of 3.9480×10^{-10}, indicating a good fit of the model to the data in that region of the graph. Figure 4.15 shows the interesting behaviour of Ψ_{WI} for values of $c \in [0, 2]$ discussed earlier. The fitting of both the curve presented in Figures 4.15 and 4.16 respectively was tackled with the help of nonlinear regression provided by the Mathematica environment [12]. In Figure 4.8 a possible fitting of the curve from Figure 4.15 is shown, where the model describing the fitting curve takes the form of

$$\Psi_{WI}(c) = s_1 + s_2\,c + s_3\,\exp\{-s_4\,c\} \quad , \tag{4.2}$$

with the model parameters s_i shown in Table 4.1. Another possible fitting of the curve in Figure 4.15 may be given by the model

$$\Psi_{WI}(c) = t_1 + t_2\,c + t_3\,\exp\{-t_4\,c - t_5\,c^2 - t_6\,c^3 - t_7\,c^4 - t_8\,c^5\} \tag{4.3}$$

shown in Figure 4.10, with the model parameters t_i defined in Table 4.2. The residuals for the model defined in Eq. 4.3 shown in Figure 4.11 display an improvement compared to the residuals in Figure 4.9 for the model from Eq. 4.2 by increasing the number of model parameters in Eq. 4.3; nonetheless, both residuals in Figures 4.9 and 4.11 respectively have trends, which actually indicates that both underlying models are not ideal for the given curve in Figure 4.15 and should be modified [13]. Figure 4.14 shows the behaviour of Ψ_{WI} with varying angle $\gamma \in (0, \pi/2)$ of the parallelepiped unit cell with the edge lengths $a = b = c = 1$ and the angles $\alpha = \beta = 90°$; in Figure 4.12 a possible fitting of the curve presented in Figure 4.16 with the use of the model

$$\Psi_{WI}(\gamma) = u_1 + u_2\,\gamma - u_3\,\exp\{-u_4\,\gamma - u_5\,\gamma^2 - u_6\,\gamma^3\} \tag{4.4}$$

is shown, with the model parameters u_i listed in Table 4.3. The residuals shown in Fig. 4.13 corresponding to the model in Eq. 4.4 show trends, indicating that the model presented in Eq. 4.3 needs to be further modified to fit the curve in Fig. 4.16 [13]. The goal was to analyze the behaviour of Ψ_{WI} with the goal to find a rather simple analytical form of Ψ_{WI} for the calculation of Ψ_{WI} depending on the unit cell size describing the unit cell.

The models presented in Eqs. 4.2, 4.3 and 4.3 each depend on a rather large number of model variables, which suggests that no simple analytical form of Ψ_{WI} may exist.

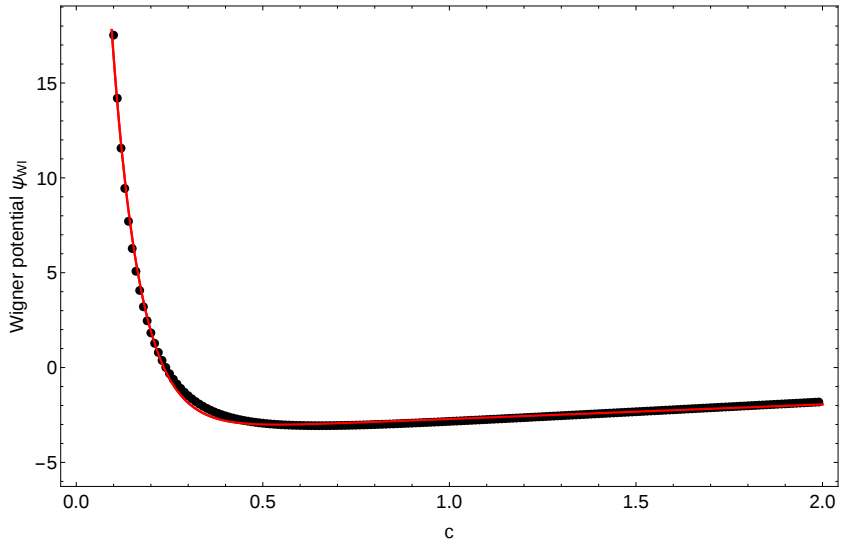

Figure 4.8: Fitting curve (red line) described by Eq. 4.2 using the parameters shown in Table 4.1 for the curve displayed in Fig. 4.15 (black line) with values $c \in [0,2], a = b = 1, \alpha = \beta = \gamma = 90°$

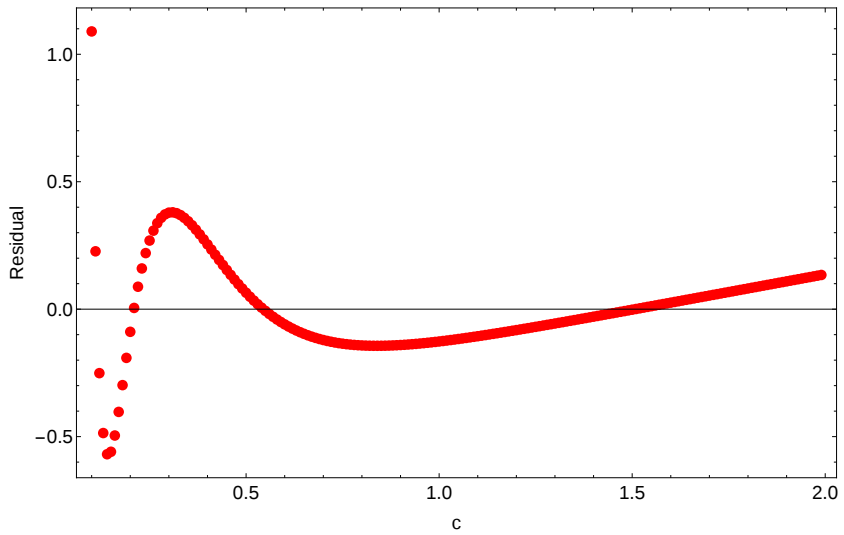

Figure 4.9: Residuals for the fitting curve described by Eq. 4.2 using the parameters shown in Table 4.1 compared to the curve in Fig. 4.15 with values $c \in [0,2], a = b = 1, \alpha = \beta = \gamma = 90°$

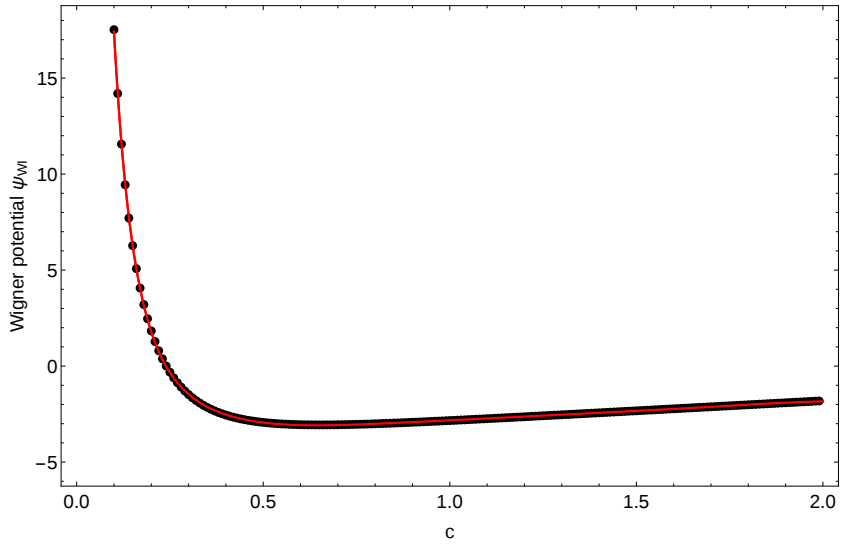

Figure 4.10: Fitting curve (red line) described by Eq. 4.3 using the parameters shown in Table 4.2 for the curve displayed in Fig. 4.15 (black line) with values $c \in [0,2], a = b = 1, \alpha = \beta = \gamma = 90°$

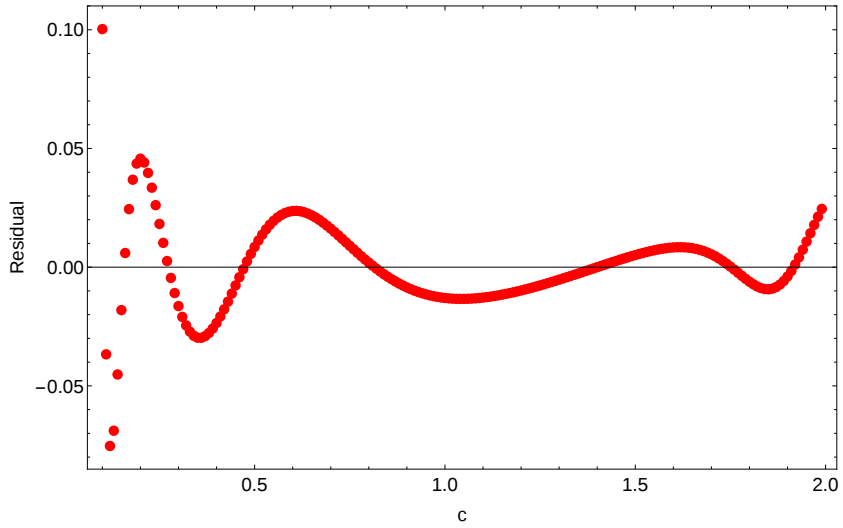

Figure 4.11: Residuals for the fitting curve described by Eq. 4.3 using the parameters shown in Table 4.2 compared to the curve in Fig. 4.15 with values $c \in [0,2], a = b = 1, \alpha = \beta = \gamma = 90°$

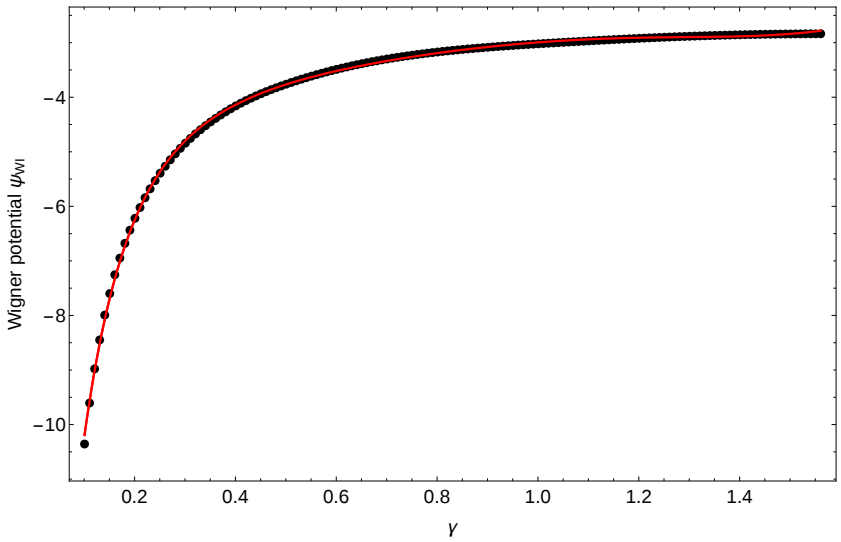

Figure 4.12: Fitting curve (red line) described by Eq. 4.4 using the parameters shown in Table 4.3 for the curve displayed in Fig. 4.16 (black line) with values $\gamma \in (0, \pi/2), a = b = c = 1, \alpha = \beta = 90°$

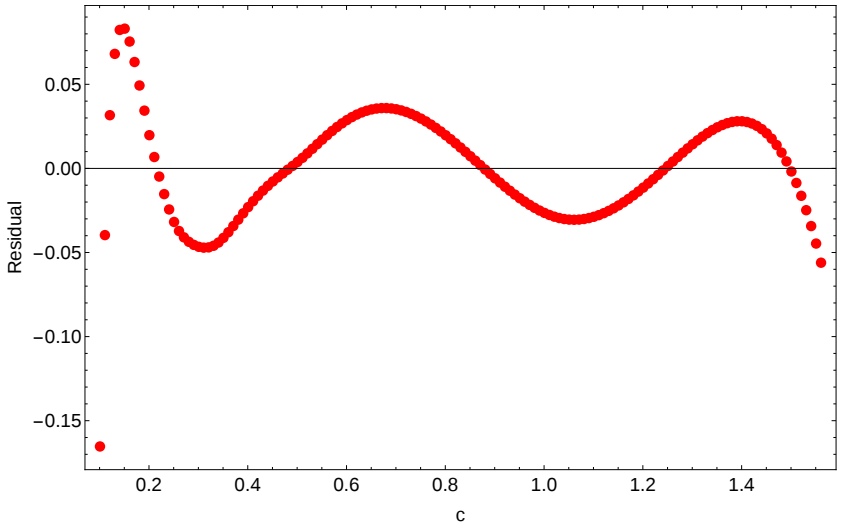

Figure 4.13: Residuals for the fitting curve described by Eq. 4.4 using the parameters shown in Table 4.3 compared to the curve in Fig. 4.16 with values $\gamma \in (0, \pi/2), a = b = c = 1, \alpha = \beta = 90°$

Table 4.1: Model parameters s_i and corresponding standard error for the model defined in Eq. 4.2 and presented in Figure 4.2

Parameter	**Standard Error**
$s_1 = -3.47856$	0.0397291
$s_2 = 0.767877$	0.0309975
$s_3 = 75.0268$	1.32703
$s_4 = 13.3042,$	0.140895

Table 4.2: Model parameters t_i and corresponding standard error for the model defined in Eq. 4.3 and presented in Figure 4.3

Parameter	**Standard Error**
$t_1 = -3.80745$	0.00864341
$t_2 = 0.9812$	0.006892
$t_3 = 179.522$	1.83128
$t_4 = 26.8539,$	0.177146
$t_5 = -63.6863$	0.992284
$t_6 = 97.0969$	2.22187
$t_7 = -62.2693$	1.76991
$t_8 = 13.4444$	0.457985

Table 4.3: Model parameters u_i and corresponding standard error for the model defined in Eq. 4.4 and presented in Figure 4.12

Parameter	**Standard Error**
$u_1 = -3.9582$	0.0351415
$u_2 = 1.4379$	0.0474756
$u_3 = 20.041$	0.252774
$u_4 = 12.5677,$	0.167667
$u_5 = -12.3504$	0.274142
$u_6 = 3.52517$	0.107532

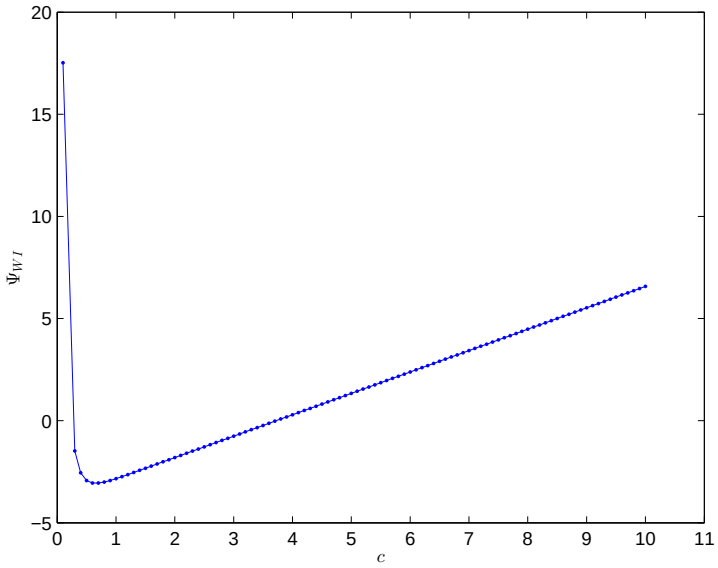

Figure 4.14: Behaviour of the Wigner potential Ψ_{WI} with varying edge length $c \in [0, 10]$, edge lengths $a = b = 1$ and angles $\alpha = \beta = \gamma = 90°$

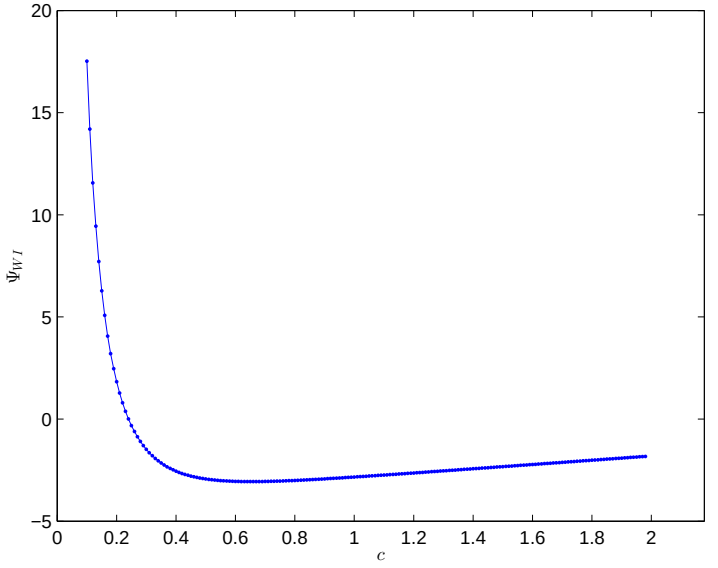

Figure 4.15: Behaviour of the Wigner potential Ψ_{WI} with varying edge length $c \in [0, 2]$, edge lengths $a = b = 1$ and angles $\alpha = \beta = \gamma = 90°$

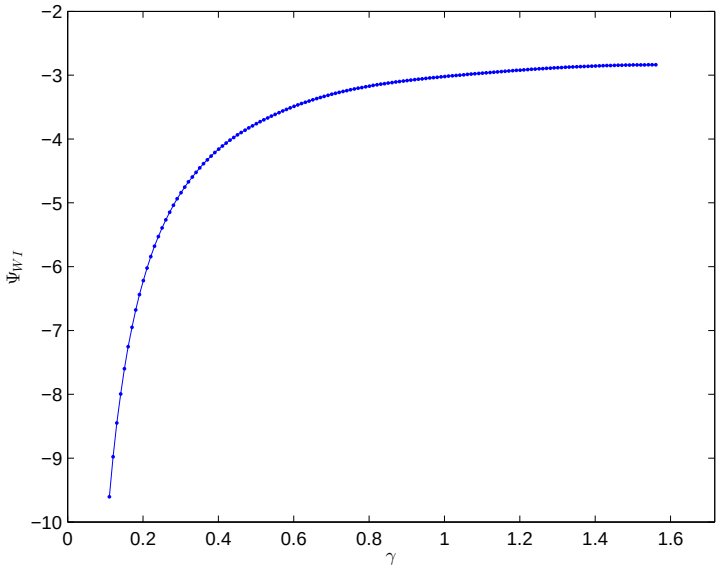

Figure 4.16: Behaviour of the Wigner potential Ψ_{WI} with varying angle $\gamma \in (0, \pi/2)$, edge lengths $a = b = c = 1$ and angles $\alpha = \beta = 90°$

Chapter 5

Conclusion

The Ewald method provides an efficient way to calculate the Wigner potential; the implementation of the Wigner potential calculation using the Ewald method showed a rather fast convergence by using only a small number of $\mathbf{l}$ vectors to converge. Further, a calculation of the optimal value for the parameter d in the calculation of the Wigner potential using the Ewald method showed to be very important; the convergence of the Wigner potential calculation depends on the right choice d_{opt} of the parameter d, which was defined as the distance to the nearest periodic neighbour. For values d greater than this optimal value tests showed a clear divergence of the Wigner potential calculation and thus a wrong numerical evaluation of the Wigner potential. Finally, the goal of this thesis was to find an analytical expression for the Wigner potential Ψ_{WI} based on the variation of the shape and size of the unit cell. The curves generated by a variation of the edge length c and by a variation of the angle γ were fitted with models approximated by a nonlinear regression. In the case of the curve resulting from the variation of the edge length c two models were approximated for the fitting of the curve; one consisting of 4 model parameters and the other consisting of 8. The increase of the number of model paramaters in this case resulted in a decrease of the maximum value of the residues; nonetheless, the approximated models were not suited for the given curve, since the residues showed a trend instead of resembling white noise. These results show that a simple analytical expression for the Wigner potential may not exist, since by only varying one parameter of the unit cell the model needed to fit the resulting curve may consist of a rather large number of model parameters, which may contradict the desired simple nature of an analytical expression for the Wigner potential.

Appendix A

Appendix

A.1 General Mathematical Definitions

A.1.1 Fourier Series Expansion

The Fourier series expansion of a function $s(\mathbf{r})$ is given by

$$s(\mathbf{r}) = V^{-1} \sum_{\mathbf{l} \in {}^t\mathbb{Z}^3} \hat{s}(\mathbf{k}) \exp\{\mathrm{i}\mathbf{k}\mathbf{r}\} \quad , \tag{A.1}$$

The Fourier coefficients $\hat{s}(\mathbf{k})$ are derived using

$$\hat{s}(\mathbf{k}) = \int\int\int_{\mathcal{C}} \mathrm{d}^3\mathbf{r} s(\mathbf{r}) \exp\{-\mathrm{i}\mathbf{k}\mathbf{r}\} \quad ; \tag{A.2}$$

$\hat{s}(\mathbf{k})$ is also called the *Fourier space version of* $s(\mathbf{k})$.

A.1.2 Fourier Coefficients of a Convolution

The convolution $(s \star t)$ of two functions s and t is defined as

$$(s \star t)(x) = \int_{-\infty}^{\infty} \mathrm{d}x' s(x') t(x - x') \quad . \tag{A.3}$$

The Fourier coefficients of the convolution shown in Eq. A.3 are related by the following simple multiplication:

$$\widehat{(s \star t)}(k) = \hat{s}(k)\hat{t}(k) \quad . \tag{A.4}$$

A.1.3 Definition of the Set $\mathcal{N}$ of Repeat Vectors for Direct Neighbours of a Charge

$$\begin{aligned}\mathcal{N} = \{&(-1,-1,-1)^\intercal, (-1,-1,0)^\intercal, (-1,-1,1)^\intercal, (-1,0,-1)^\intercal, (-1,0,0)^\intercal,\\ &(-1,0,1)^\intercal, (-1,1,-1)^\intercal, (-1,1,0)^\intercal, (-1,1,1)^\intercal, (0,-1,-1)^\intercal,\\ &(0,-1,0)^\intercal, (0,-1,1)^\intercal, (0,0,-1)^\intercal, (0,0,1)^\intercal, (0,1,-1)^\intercal, (0,1,0)^\intercal,\\ &(0,1,1)^\intercal, (1,-1,-1)^\intercal, (1,-1,0)^\intercal, (1,-1,1)^\intercal, (1,0,-1)^\intercal,\\ &(1,0,0)^\intercal, (1,0,1)^\intercal, (1,1,-1)^\intercal, (1,1,0)^\intercal, (1,1,1)^\intercal\} \quad ,\end{aligned} \tag{A.5}$$

with $|\mathcal{N}| = 26$.

A.2 Source Code

A.2.1 Implementation of the Wigner Potential Calculation in a Crystal System Represented by a Cubic Unit Cell of Length L Using a Direct Sum [3]

Listing A.1: Implementation of the Wigner potential calculation in a crystal system represented by a cubic unit cell of length L using a direct sum [3]

```
double ewald_self_cube_direct(double L, int lmax) {
  int lx, ly, lz, l2;
  double kx, ky, kz, k2, rk;

  double bx = L;
  double by = L;
  double bz = L;
  double vol = bx*by*bz;

  int lmax2 = lmax*lmax;

  double pi = 4.0*atan2(1.0,1.0);

  double sum = 0.0;

  for ( lx = -lmax; lx <= lmax; lx++ ) {
    for ( ly = -lmax; ly <= lmax; ly++ ) {
      for ( lz = -lmax; lz <= lmax; lz++ ) {
l2 = lx*lx + ly*ly + lz*lz;
if ( ( lx !=0 || ly != 0 || lz != 0 ) && l2 <=
   ↪ lmax2 ) {
  kx = (2.0*pi/bx)*lx;
```

```
    ky = (2.0*pi/by)*ly;
    kz = (2.0*pi/bz)*lz;
    k2 = kx*kx + ky*ky + kz*kz;
    sum += 1.0/k2;
  }
      }
    }
  }

  sum -= L*L*lmax/pi;

  sum *= 4.0*pi/vol;
  return sum;
}
```

A.2.2 Implementation of the Wigner Potential Calculation in Crystal Systems Using the Ewald Method

Listing A.2: Implementation of the Wigner potential calculation in crystal systems using the Ewald method

```
double calc_wigner_potential_ewald(Matrix<double>& L,
   ↪  double d, int lmax) {
  assert(L.size1() == 3);
  assert(L.size2() == 3);

  Matrix<double> L_inv(L.size1(), L.size2());

  inverse_33(L,L_inv);

  vector<double> l(3);
  vector<double> k(3);

  int lmax2 = lmax*lmax;
  int l_length_sqr = 0;
  double k_length_sqr = 0;
  double d_k = 0;
  double sum = 0;
  double vol = abs(determinant_33(L));

  for (int lx = -lmax; lx <= lmax; lx++ ) {
    for (int ly = -lmax; ly <= lmax; ly++ ) {
      for (int lz = -lmax; lz <= lmax; lz++ ) {
        l_length_sqr = lx*lx + ly*ly + lz*lz;
```

```
        if ( ( lx !=0 || ly != 0 || lz != 0 ) &&
           ↪ l_length_sqr <= lmax2 ) {
          l[0] = lx;
          l[1] = ly;
          l[2] = lz;

          vm_multiplication(l, L_inv, k);
          sv_multiplication(2*M_PI, k);

          k_length_sqr = k[0] * k[0] + k[1] * k[1] +
             ↪ k[2] * k[2];

          d_k = d * sqrt(k_length_sqr);
          sum += 12.0/(d_k * d_k * d_k * d_k) * (2.0
             ↪ - 2.0* cos(d_k) - d_k * sin(d_k)) /
             ↪ k_length_sqr;
        }
      }
    }
  }

  sum *= 4.0 * M_PI / vol;
  sum += -(4.0 / 15.0) * M_PI / vol * d * d - 2.0 / d
     ↪ ;

  return sum;
}
```

A.2.3 Implementation of the Calculation of d_{opt} for a Parallelepiped Unit Cell

Listing A.3: Implementation of the calculation of d_{opt} based on the parameters $a, b, c, \alpha, \beta, \gamma$ describing the parallelepiped unit cell

```
double calc_min_distance(double a, double b, double c
   ↪ , double alpha, double beta, double gamma){
  vector<coord_3d> nearest_neighbors_coords(26);
  double step_size = 1;
  int i = 0;
  coord_3d coord;

  /*
    Set up coordinates of the neareast neighbors of
       ↪ the charge q
    at the origin of the coordinate system
```

```
*/
for (double x = -1; x <= 1; x+=step_size)
{
  for (double y = -1; y <= 1; y+=step_size)
  {
    for (double z = -1; z <= 1; z+=step_size)
    {
      coord.x = x;
      coord.y = y;
      coord.z = z;

      if(x == 0 && y == 0 && z == 0)
        continue;

      nearest_neighbors_coords[i] = coord;
      i++;
    }
  }
}

Matrix<double> L(3,3);
get_unit_cell_size_parallelepiped(a, b, c, alpha,
   ↪ beta, gamma, L);

vector<double> coord_cart(3);
vector<double> coord_fract(3);

double min_distance = DBL_MAX;
double curr_distance = 0;

for (int i = 0; i < nearest_neighbors_coords.size()
   ↪ ; ++i)
{
  coord_fract[0] = nearest_neighbors_coords[i].x;
  coord_fract[1] = nearest_neighbors_coords[i].y;
  coord_fract[2] = nearest_neighbors_coords[i].z;

  // Transform fractional coordinates to cartesian
     ↪ coordinates
  mv_multiplication(L, coord_fract, coord_cart);

  curr_distance = sqrt((coord_cart[0]*coord_cart
     ↪ [0])
          + (coord_cart[1]*coord_cart[1])
```

```
            + (coord_cart[2]*coord_cart[2]));

    if(curr_distance < min_distance)
      min_distance = curr_distance;
  }

  return min_distance;
}
```

Bibliography

[1] Donald R Askeland and Pradeep Prabhakar Phulé. The science and engineering of materials. 2003.

[2] Wikimedia Commons. Image of a crystal unit cell definition. http://commons.wikimedia.org/wiki/File:UnitCell.png, 2008.

[3] Philippe H Hünenberger. Implementation of the wigner potential calculation in a crystal system represented by a cubic unit cell of length l.

[4] Philippe H Hünenberger. Optimal charge-shaping functions for the particle–particle—particle–mesh (p3m) method for computing electrostatic interactions in molecular simulations. The Journal of Chemical Physics, 113(23):10464–10476, 2000.

[5] Philippe H Hünenberger. Lattice-sum methods for computing electrostatic interactions in molecular simulations. In Simulation and theory of electrostatic interactions in solution, volume 492, pages 17–83. AIP Publishing, 2008.

[6] Philippe H Hünenberger. Private communication, 2014.

[7] Andrew R. Leach. Molecular modelling: principles and applications. Pearson Education, 2001.

[8] Hark Lee and Wei Cai. Ewald summation for coulomb interactions in a periodic supercell. Lecture Notes, Stanford University, 2009.

[9] Brock A Luty, Ilario G Tironi, and Wilfred F van Gunsteren. Lattice-sum methods for calculating electrostatic interactions in molecular simulations. The Journal of Chemical Physics, 103(8):3014–3021, 1995.

[10] Erik M Olsen. Green's functions and their applications in physics. vol, 1200:1–4, 2008.

[11] Bernhard Rupp. Biomolecular crystallography: principles, practice, and application to structural biology. Garland Science, 2009.

[12] Martin Suter. Private communication, 2014.

[13] Martin Suter. Private communication, 2015.

[14] Eric W. Weisstein. Cramer's rule. From MathWorld—A Wolfram Web Resource. http://mathworld.wolfram.com/CramersRule.html.